Direct Numerical Experiment on Two-Dimensional Pinning Dynamics of a Three-Dimensional Vortex Line in Layered Superconductors

Masahiko Machida* and Hideo Kaburaki

Computing and Information Systems Center, Japan Atomic Energy Research Institute, Tokai-mura, Naka-gun, Ibaraki 319-11, Japan

(Received 30 May 1995)

We clarify structures and dynamics of tilted vortices in the T_c modulated three-dimensional (3D) layered superconductor by performing a direct numerical simulation of the time-dependent Ginzburg-Landau equation coupled with Maxwell's equation. The change of vortex dynamics from a rigid and straight vortex line in the low temperature region to a stepwise vortex in the high temperature region is observed. We investigate vortex pinning for columnar and point defects, and find that a flexible deformation of vortex segments parallel to the layer in the 3D continuous stepwise vortex is reinforced in the presence of pinning centers and leads to 2D pinning dynamics. Also, this increased flexibility is shown to bring about more effective vortex pinning.

PACS numbers: 74.60.Ge, 74.80.Dm

The mixed states in high temperature superconductors (HTSC's) have been extensively studied in recent years, where one of the primary concerns is quasi-2D vortex dynamics in intrinsic layered crystal structures [1]. Vortex models have been proposed to explain this reduced dimensionality in dynamics. For weakly anisotropic HTSC's such as $YBa_2Cu_3O_{7-\delta}$ (YBCO), Tachiki and Takahashi [2] suggested a stepwise vortex and two pinning mechanisms, which are intrinsic pinning due to the vortex segment parallel to the layer and extrinsic pinning due to that perpendicular to the layer. On the other hand, Kes *et al.* [3] and Clem [4] introduced a 2D pancake vortex localized in the CuO_2 layer for highly anisotropic (Josephson-coupled) HTSC's such as $Bi_2Sr_2CaCu_2O_{8+\delta}$ (BSCCO), and proposed the extrinsic pinning by this 2D vortex. In the former model, continuous 3D flux lines piercing through the sample are assumed, while the latter model considers a stack of discrete 2D pancake vortices existing in different CuO_2 layers for the description of vortex states. In fact, in weakly anisotropic HTSC's, such as YBCO, there exist experimental data [5] for the dependence of the critical current $J_c(\theta)$ on the angle θ between the magnetic field and the c axis, which are in good agreement with the stepwise vortex model, whereas, for highly anisotropic HTSC's, such as BSCCO [6] and $Nd_{1.85}Ce_{0.15}CuO_{4-\delta}$ [7], many data on the behavior of $J_c(\theta)$ are consistent with the 2D pancake vortex model except in the high temperature region. Moreover, in the artificial superlattice composed of YBCO and $Pr_xY_{1-x}Ba_2Cu_3O_{7-\delta}$ (PrYBCO) where each material has its different T_c [T_c(PrYBCO) $< T_c$(YBCO)], the 3D-2D crossover on flux pinning has been reported using both the stepwise vortex model and the 2D pancake vortex model in the temperature range below and above $T = T_c$(PrYBCO) [8]. This 3D-2D crossover has also been observed in the fully oxidized YBCO (FO-YBCO), in which the CuO plane and chain layer are considered to have different T_c's [9]. Although there exist many experimental data that support two models, it is still not clear whether vortex dynamics in HTSC's, PrYBCO/YBCO, and FO-YBCO are really represented by the continuous 3D stepwise vortex line and discrete 2D (coupled or decoupled) vortex. Therefore our purpose is to investigate vortex features in those 3D and 2D vortex dynamics behaviors and to propose a possible description of vortex features in HTSC's. In this paper, we focus on YBCO/PrYBCO and FO-YBCO and perform a direct numerical simulation [10] using the time-dependent Ginzburg-Landau (TDGL) equation. In our simulations, the TDGL and Maxwell equations are discretized using the link variable $e^{i\int^{\mathbf{A}\cdot d\mathbf{l}}}$ instead of the vector potential $\mathbf{A}$, and time derivatives of both equations are integrated by the Euler method. Generally, within the framework of the GL or TDGL theory, the layered structures of HTSC's have been described by models such as the anisotropic effective mass model [11] for weakly anisotropic HTSC's and the Lawrence-Doniach model [12] for highly anisotropic (Josephson coupled) HTSC's. In this paper, we neglect effective mass anisotropy and concentrate only on the modulation of T_c since the target materials YBCO/PrYBCO and FO-YBCO are weakly anisotropic superconductors, and a main characteristic of those materials is the variation of T_c. The equation employed for the modulation of T_c is $T_c = T_m + T_v \cos[(2\pi/d)z]$, where T_m and T_v are 20 and 10 K, respectively. It is considered that this model corresponds to a superlattice composed of two superconducting materials in which $T_c = 30$ K and $T_c = 10$ K, and a coupling between layers gives rise to the sinusoidal modulation of T_c. If the measuring temperature T is assumed to be below and above T_c(min) (= 10 K), S-S' and S-N type superconducting multilayers can be realized, respectively, by this simple layered model. Also, a layered model with $d = 8\xi(0)$, in which d is the periodicity of the layer, is used in all simulations. This condition fully corresponds to the layered character of YBCO/PrYBCO or FO-YBCO. The

 0031-9007/95/75(17)/3178(4)$06.00

spatial modulation of T_c and the computational region are shown in the inset of Fig. 1. For numerical simulations, the method is found in Ref. [10]. The boundary conditions $[\nabla/i - (2e/\hbar c)\mathbf{A}]^2\psi|_n = 0$ for the TDGL equation and $\mathbf{B} = \mathbf{H}_a + \mathbf{H}_i$ for the Maxwell equation are introduced. Here, $|_n$ is the normal direction at the free boundary surface, and $\mathbf{H}_a$ and $\mathbf{H}_i$ are the applied magnetic field and the current induced magnetic field as shown in the inset of Fig. 1. The $\mathbf{H}_i$ can be calculated by Ampere's law as follows: $\int_C \mathbf{H}_i \cdot d\boldsymbol{l} = \int_S \mathbf{i}\, dS$, where C and S in the inset of Fig. 1 correspond to the path of the line integral and the cross section perpendicular to the current direction, respectively. In all simulations, the GL parameter is 2, and the minimum mesh and time step are $0.5\xi(0)$ and 0.01, respectively. The size of the computational region is $40\xi(0) \times 40\xi(0) \times 20\xi(0)$, and the applied field is tilted 45° from the c direction. Also, the thermal noise for both equations is neglected.

First, we show the H-T diagram of the vortex structures and characteristic distributions of the order parameter corresponding to each phase in Fig. 1. It is found that the vortex state can be classified into region I and region II

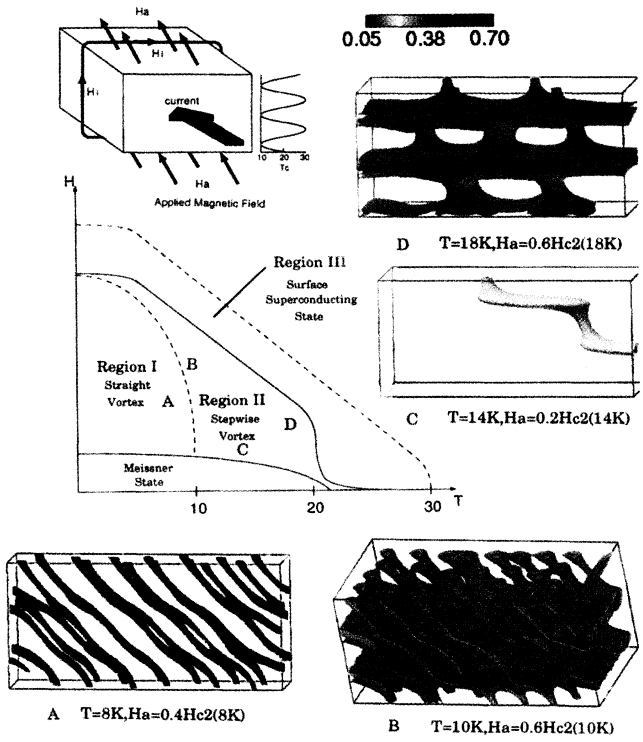

FIG. 1. The H-T diagram of the vortex structure and computational region of a rectangular parallelpiped conductor. The periodicity d of T_c is $8\xi(0)$, and $\mathbf{H}_a$ and $\mathbf{H}_i$ are the applied magnetic field and the current-induced magnetic field, respectively. $\mathbf{H}_a$ is tilted 45° from the c direction, and the direction of the current is shown in the figure. The insets represent the characteristic order parameter distributions of the steady vortex states. The alphabet indicates the position in the H-T diagram.

due to the difference of vortex structures. In region I, where $T < 10$ [$= T_c(\min)$], straight flux lines or slightly modulated flux lines are observed as shown in inset A of Fig. 1. On the other hand, in region II, where $T > 10$ [$= T_c(\min)$], vortices are strongly modulated by the layered structure, and a complete stepwise vortex, which is composed of segments parallel and perpendicular to the layer, is observed as shown in insets C and D of Fig. 1. Here, it should be noted that in spite of $T > 10$ [$= T_c(\min)$], the amplitude of the order parameter in the weak superconducting layer with $T_c(\min)$ shows a nonzero value due to the proximity effect by stronger superconducting layers. In this model, up to the boundary line between regions II and III (surface superconducting state) as shown in Fig. 1, only the continuous 3D stepwise vortex is observed because the proximity effect induces 3D superconducting coupling. Just above the boundary line, large normal regions formed by merging many vortices are found to spread rapidly except for the surface boundary.

Next, let us consider free flux flow without pinning centers. Two snapshots of the flux flow of a stepwise vortex and a straight vortex are shown in Figs. 2(a) and 2(b), where the open arrow and the solid arrow indicate the direction of the moving vortex and the direction of the Lorentz force, respectively. Here, the numerical conditions are shown in the caption of each figure. It is found that straight vortex lines move in the direction of the Lorentz force as $\mathbf{F}_L = \mathbf{B} \times \mathbf{J}$, while for the stepwise vortex, both vortex segments perpendicular and parallel to the layer move only in the direction parallel to the layer. This is because the strong intrinsic pinning perfectly prevents the vortex segment parallel to the layer from moving in the direction of the Lorentz force. Therefore the main dissipation arises from the vortex segment perpendicular to the layer. With these behaviors, it is found in the absence of vortex pinning that a crossover from the 3D straight vortex dynamics to the 3D stepwise vortex dynamics occurs at the boundary between regions I and II.

Second, let us consider the vortex dynamics in the presence of columnar defects [13–18]. In the numerical simulation, the columnar defect in the direction of the c axis is realized as a cylindrical region in which $T_c = 0$, and the radius size is $2.0\xi(0)$. Two snapshots of the distribution of the order parameter at $T = 14$ K are shown in Figs. 3(a) and 3(b), in which Fig. 3(b) corresponds to the snapshot after 60 000 time steps from the result of Fig. 3(a). Here, with the constant current exceeding J_c, it is shown that perpendicular segments of a stepwise vortex move parallel to the layer and reiterate the pinning and depinning process alternatively, while parallel vortex segments extend or contract flexibly according to the movement of perpendicular vortex segments. This fact implies that the pinning by a columnar defect works only for the perpendicular segments, and even in the case

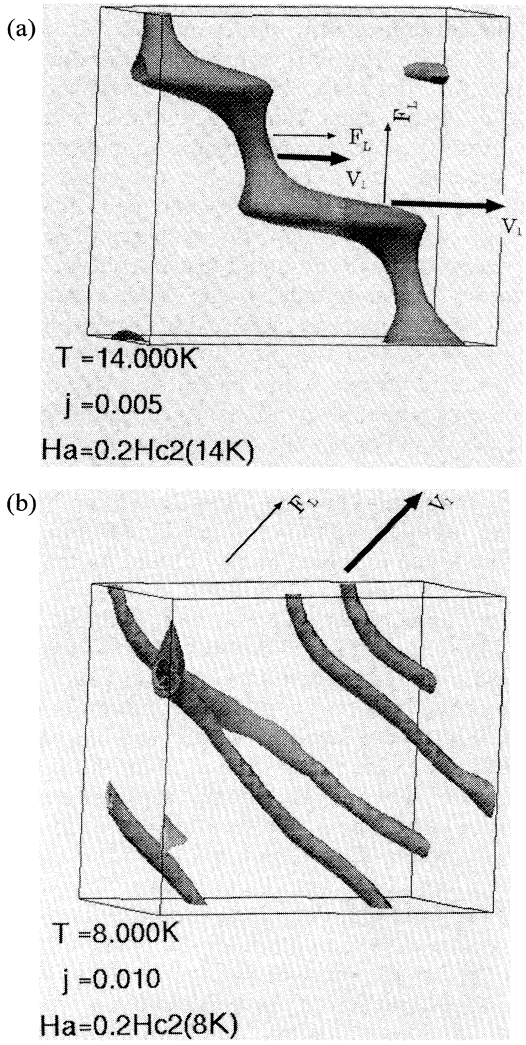

FIG. 2. (a) The enlarged view of the moving vortex. The numerical conditions are shown in the figure. The light arrow and bold arrow indicate the direction of Lorentz force and moving vortex. (b) The enlarged view of the moving vortex. The numerical conditions are shown in the figure. The light arrow and bold arrow indicate the direction of Lorentz force and moving vortex.

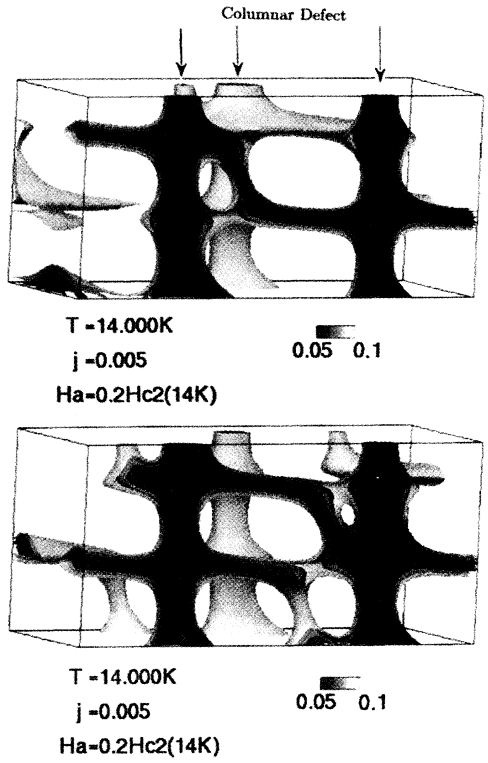

FIG. 3. (a) The enlarged view of moving vortices and columnar defects. The numerical conditions are shown in the figure. (b) The snapshot after 60 000 times steps from the result of (a).

of finite angle between the direction of the columnar defect and the magnetic field, the pinning by the columnar defect remains to be effective [14,15]. On the other hand, Fig. 4 shows a snapshot of the distribution of the order parameter at $T = 6$ K. The pinning by a columnar defect at this temperature is found to be ineffective in the case of the finite angle between the magnetic field and the columnar defect since pinning volumes by the movement of vortices do not change greatly [13,16,17]. It follows from these results that the angular dependence of the pinning dynamics by columnar defects exhibits a crossover from 3D to quasi-2D vortex behavior at the temperature of $T = T_{c\min}$. With these results, one can say that a flexible change of the length of the parallel vortex segment in one layer gives rise to quasi-2D vortex dynamics behaviors with retaining features of a 3D continuous vortex line.

Third, let us consider the pinning by point defects [19,20]. Here, the shape of the point defect is assumed to be cubic, in which the length of one side is $2.0\xi(0)$, and it is realized as the region with $T_c = 0$ K. Figure 5 shows a snapshot of the order parameter distribution, in the presence of point defects at 14 K. It is observed

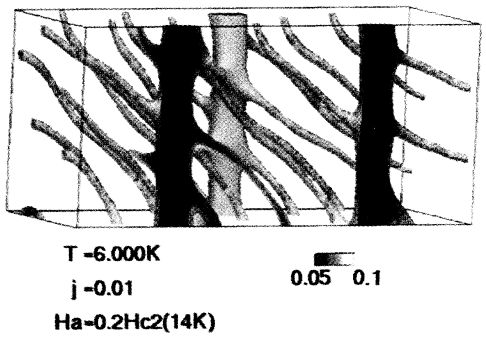

FIG. 4. The enlarged view of the moving vortices and columnar defects. The numerical conditions are shown in the figure.

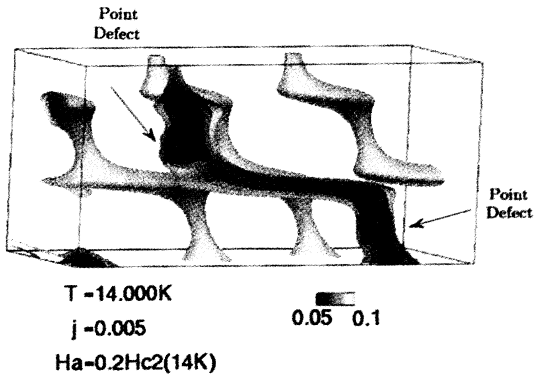

FIG. 5. The enlarged view of the moving vortices and the cubic-shaped point defects. The numerical conditions are shown in the figure.

in the figure that the pinned vortex is strongly deformed compared with other free flow vortices. It is found that the strong point pinning in the high-temperature region II is extremely effective due to the flexible deformation of a stepwise vortex. By observing the vortex dynamics in the presence of these two types of strong pinning centers, it is predicted that the pinning dynamics of the 3D continuous vortex line with flexibly deformed segments is roughly equivalent to that of the decoupled 2D vortex. It should be noted that quasi-2D vortex dynamics can be formed only in the condition that the pinning energy is sufficiently larger than the deformation energy for layer-parallel segments.

In conclusion, the perpendicular segment of a stepwise vortex is mainly responsible for the pinning and dissipation, while the parallel component only contributes to the deformation of the vortex line. Also, in the presence of the pinning center, we found that the vortex is more deformed, and this deformation leads to effective pinning for a vortex line and layer-independent quasi-2D vortex dynamics. We would like to point out that the 2D behaviors on vortex pinning dynamics in HTSC's can be understood on the basis of a continuous 3D vortex line with flexible layer-parallel segments.

We thank K. Kato for computer graphics.

*On leave from FUJITSU Ltd., Izumi-Cho 1-2-4, Mito-Shi Ibaraki-Ken, 310, Japan.

[1] G. Blatter *et al.,* Rev. Mod. Phys. **66**, 1125 (1994).
[2] M. Tachiki and S. Takahashi, Solid State Commun. **72**, 1083 (1989).
[3] P. H. Kes *et al.,* Phys. Rev. Lett. **64**, 1063 (1990).
[4] John R. Clem, Phys. Rev. B **43**, 7837 (1991).
[5] B. Roas *et al.,* Phys. Rev. Lett. **64**, 479 (1990).
[6] P. Shmitt *et al.,* Phys. Rev. Lett. **67**, 267 (1991).
[7] M. Rajeswari, Physica (Amsterdam) **229C**, 258 (1994).
[8] Qi. Li *et al.,* Phys. Rev. Lett. **69**, 2713 (1992).
[9] Z. X. Gao *et al.,* Phys. Rev. Lett. **71**, 3210 (1993).
[10] M. Machida and H. Kaburaki, Phys. Rev. Lett. **74**, 1434 (1995).
[11] V. G. Kogan, Phys. Rev. B **38**, 7049 (1988).
[12] W. E. Lawrence and S. Doniach, in *Proceedings of the 12th International Conference on Low Temperature Physics*, edited by E. Kanda (Academic Press of Japan, Kyoto, 1971), p. 361.
[13] L. Civale *et al.,* Phys. Rev. Lett. **67**, 648 (1991).
[14] J. R. Thompson *et al.,* Appl. Phys. Lett. **60**, 2306 (1992).
[15] B. Holzapfel *et al.,* Phys. Rev. B **48**, 600 (1993).
[16] R. Prozorov *et al.,* Physica (Amsterdam) **234C**, 311 (1994).
[17] L. Klein *et al.,* Phys. Rev. B **48**, 3523 (1993).
[18] T. Schuster and H. Kuhn, Phys. Rev. B **51**, 16358 (1995).
[19] V. V. Metlushko *et al.,* Europhys. Lett. **10**, 371 (1994).
[20] V. V. Moshchalkov *et al.*. Phys. Rev. B **50**, 639 (1994).

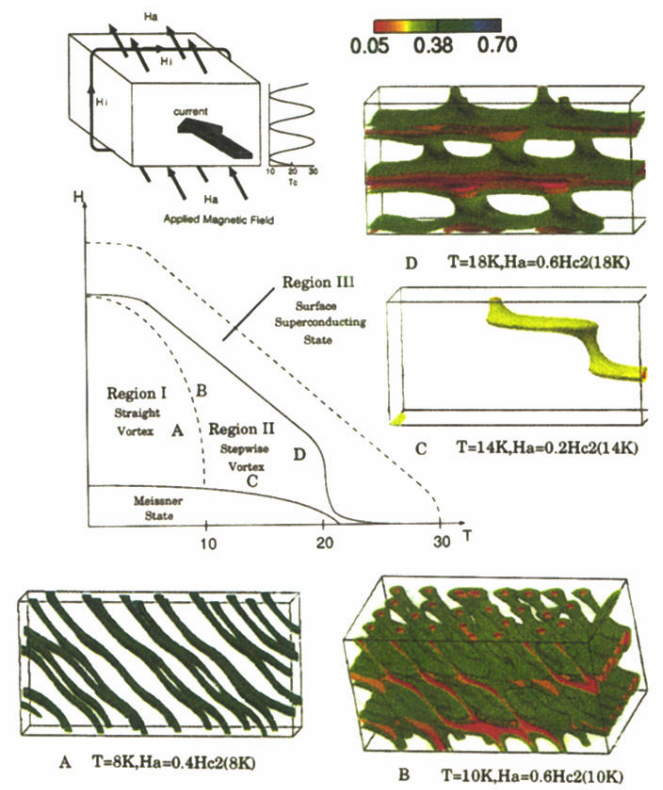

FIG. 1. The H-T diagram of the vortex structure and computational region of a rectangular parallelpiped conductor. The periodicity d of T_c is $8\xi(0)$, and $\mathbf{H}_a$ and $\mathbf{H}_i$ are the applied magnetic field and the current-induced magnetic field, respectively. $\mathbf{H}_a$ is tilted 45° from the c direction, and the direction of the current is shown in the figure. The insets represent the characteristic order parameter distributions of the steady vortex states. The alphabet indicates the position in the H-T diagram.

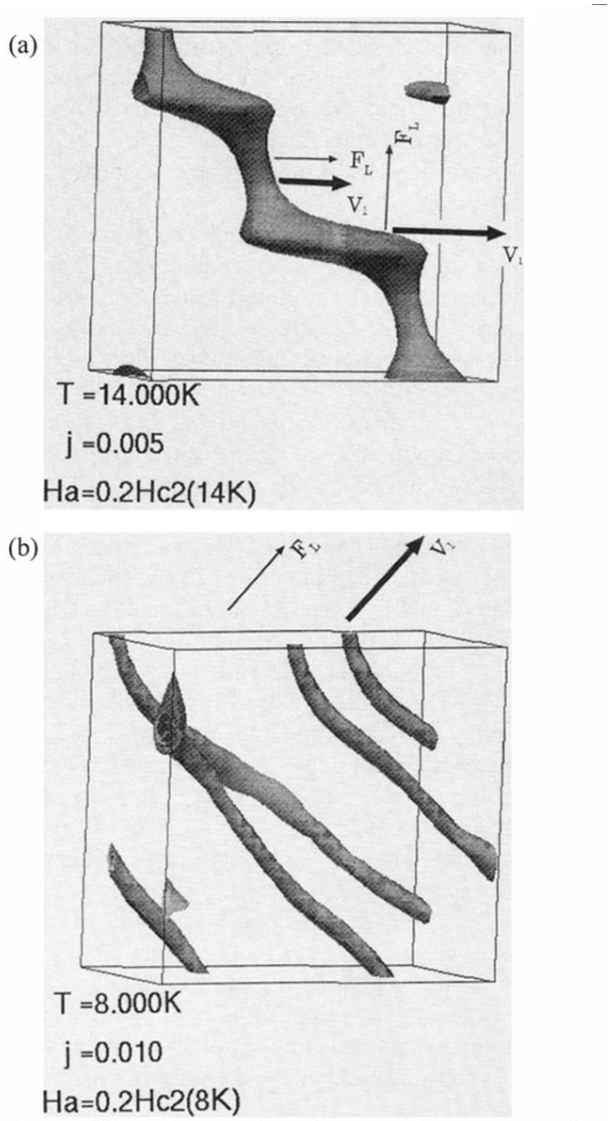

FIG. 2. (a) The enlarged view of the moving vortex. The numerical conditions are shown in the figure. The light arrow and bold arrow indicate the direction of Lorentz force and moving vortex. (b) The enlarged view of the moving vortex. The numerical conditions are shown in the figure. The light arrow and bold arrow indicate the direction of Lorentz force and moving vortex.

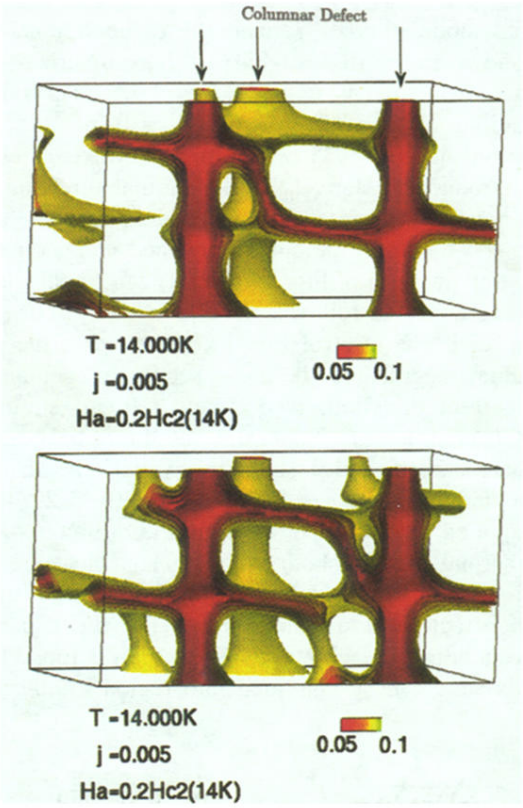

FIG. 3. (a) The enlarged view of moving vortices and columnar defects. The numerical conditions are shown in the figure. (b) The snapshot after 60 000 times steps from the result of (a).

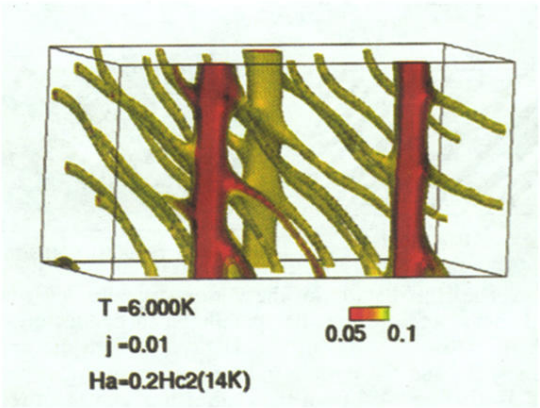

FIG. 4. The enlarged view of the moving vortices and columnar defects. The numerical conditions are shown in the figure.

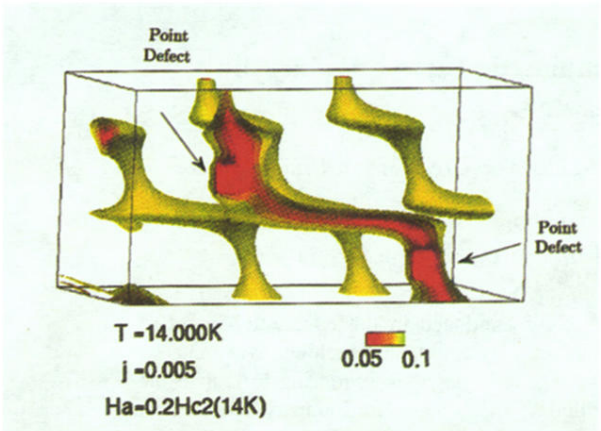

FIG. 5. The enlarged view of the moving vortices and the cubic-shaped point defects. The numerical conditions are shown in the figure.